



Available online at www.sciencedirect.com

ScienceDirect

Proceedings
of the
Combustion
Institute

Proceedings of the Combustion Institute 39 (2023) 2817–2824

www.elsevier.com/locate/proci

The effects of flame generated turbulence for turbulent-induced deflagration to detonation transition

Rachel Hytovick, Cal Rising, Anthony Morales, Tommy Genova, Joshua Berson, Kareem Ahmed*

University of Central Florida, Orlando, FL 32828, United States.

Received 6 January 2022; accepted 2 September 2022 Available online 16 November 2022

Abstract

The turbulent deflagration to detonation transition (DDT) process occurs when a subsonic flame interacts with intense turbulence resulting in spontaneous acceleration and the onset of DDT. The mechanisms that govern the spontaneous ignition are deduced intricately in numerical simulations. This work experimentally explores the conditions that are known precursors to detonation initiation. More specifically, the experiment presented investigates the role of flame-generated compression as a cycle that continuously amplifies until a hotspot forms on the flame front and ignites. The study quantifies the compression comparatively against other flame regimes through ultra-high speed pressure measurements while qualitatively detailing flame generated compression through density gradients via schlieren imaging. Additionally, flow field measurements are quantified throughout the flow using simultaneous particle image velocimetry (PIV) and OH* chemiluminescence. The turbulence fluctuations and flame speeds are extracted from these measurements to identify the reactant conditions where flame-generated compression begins. Collectively, these simultaneous high-speed measurements provide detailed insight into the flame and flow field characteristics where the runaway process occurs. This work ultimately documents direct flow field measurements to extract the contribution of flame-generated turbulence on the turbulent deflagration to detonation transition process.

© 2022 The Combustion Institute. Published by Elsevier Inc. All rights reserved.

Keywords: Pressure Gain Combustion; Deflagration to Detonation Transition

1. Introduction

The deflagration to detonation transition (DDT) process occurs when a subsonic flame un-

E-mail address: kareem.ahmed@ucf.edu (K. Ahmed).

dergoes rapid flame acceleration until it becomes a propagating detonation [1]. Witnessed frequently in pressure gain combustion applications, interstellar combustion and occasionally in chemical gas explosions, the importance of understanding the governing mechanisms of DDT cannot be underestimated [2,3]. While the transition process has been well documented in previous research, the mechanisms of turbulence-induced acceleration require further study [4,5]. One mechanism

^{*} Corresponding author at: University of Central Florida, Mechanical and Aerospace Engineering, Eng. 1, Rm. 217, Orlando, Florida 32828, United States.

thought to drive the DDT process is turbulent flame compressibility, which can lead to significant flame generated turbulence [6]. The increased turbulence generated alters the flame and flow field which requires further investigation for a thorough understanding of the turbulence and flame interactions throughout the turbulence-induced DDT process.

To better understand this specific transition process, it is important to examine the compressible turbulence and the resulting flame dynamics for each flame regime. Traditionally, flames are described in three regimes: (1) slow deflagrations, where flames propagate at subsonic velocities with a uniform V structure and propagate at a rate slower than the CJ deflagration speed, (2) fast deflagrations, where normal shock produces compression and flames travel below the isobaric speed of sound leading the flame to travel near the CJ deflagration speed, and (3) choked flames, that occur when the isobaric speed of sound has been exceeded and the runaway mechanism is induced when the flame speed is faster than the CJ deflagration speed [6,7]. These regimes have been explored both numerically and experimentally [5,8,9]. More specifically, the fast deflagration region has been investigated for its "preconditioning" characteristics that define the precursing attributes required for turbulent flame acceleration. Once conditions for spontaneous transition have been met, non-linear compressibility is known to occur and incite further acceleration [10]. The results of this acceleration lead to the deflagration to detonation transition where the pressure gain experienced by the flow becomes advantageous [11].

Several previous studies have focused on examining the flame and flow-field interactions to provide insight into DDT onset [4,12-14]. Recently Ogawa et al. conducted a numerical study of DDT in an array of cylinders using adaptive mesh refinement [15]. They witnessed significant vortex shedding and approximately 25 times expansion in the flame surface area in DDT cases. This indicates that highly perturbed flame fronts are a strong predictor of DDT onset. Additionally, Wang et al. conducted another numerical study examining the boundary layer effects on flame acceleration [16–18]. They also noted significant wrinkling of the flame front prior to DDT. In both studies, the wrinkling is attributed to turbulence induced flame-vortex interactions coupled with an increase in pressure immediately ahead of the flame. From an experimental and numerical standpoint, Xang et al. explored flame acceleration from a shock interacting with a flame front. The experimental results agreed with numerical simulations that turbulent flame elongation is a significant contributor to DDT [19]. These studies demonstrate the importance of understanding the flame turbulence interactions which should be extended to the other flame regimes to understand the DDT process.

In the last decade, there have been significant contributions in defining DDT characteristics via flow field measurements [20]. Poludnenko et al. defined a relationship for dictating the runaway boundary for turbulent flames through a proposed Chapman-Jouguet deflagration speed [21,22]. It was concluded that once the flame was propagating at a speed that exceeded the CJ deflagration velocity, the spontaneous flame acceleration occurs and the DDT process occurs; i.e., $S_{CJ} = c_{\{s,p\}}/\alpha$, where c_{s,p} is the speed of sound in the product region and α is the density ratio between the fuel and the combustion products. An experiment conducted by Sosa et al., provided experimental confirmation of this relationship while also revealing the nonlinear compressibility found in turbulent fast flames [23]. These flow field investigations support the characteristics defined for each regime as slow deflagrations are known to have low turbulent flame speeds, fast deflagrations begin to approach the CJ deflagration speed, and choked flames typically exceed

The existing literature has primarily consisted of numerical studies focused on the DDT phenomena [24]. The current study experimentally characterizes the flame-turbulence interactions of the flame acceleration regimes leading up to DDT. The objective is to further understand the flame compressibility dynamics leading to flame acceleration. This is done by utilizing simultaneous schlieren, chemiluminescence, particle image velocimetry (PIV), and pressure measurements in a turbulent shock tube facility. The results highlight the importance of the flame generated compressed region formed in front of the flame, which is shown to cause augmented turbulence and vorticity leading to the spontaneous acceleration of turbulent compressible flames for DDT.

2. Methodology

2.1. Experimental facility

The experimental facility is shown in Fig. 1. The facility, known as the Turbulent Shock Tube (TST), is housed at the Propulsion and Energy Research Laboratory at University of Central Florida [11,22,25-27]. The TST is a 45 mm square channel composed of 12 mm thick stainless steel and is 1.5 m long. The facility is made up of four sections: initiator, turbulence generator, test section, and straight open section. The initiator is located at the closed end of the TST and contains eight premixed inlets that surround a spark plug ignition source. Immediately downstream of the initiator is a 102 mm long channel, which leads into a 610 mm long turbulence generator. The turbulence generator includes six perforated plates with the last perforated plate at the entrance of the test section act to generate isotropic turbulence in

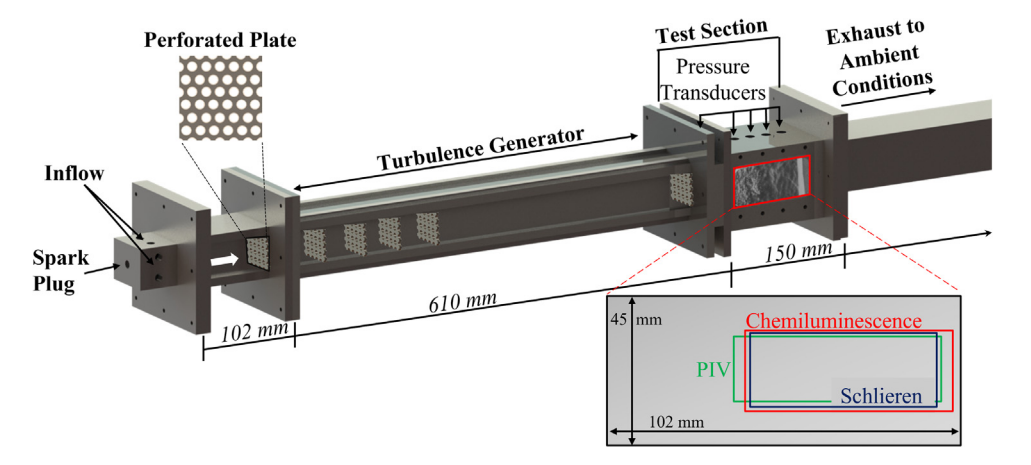


Fig. 1. Experimental facility and corresponding fields of view for various optical diagnostics.

the reactant region in front of the flame through choked jets, and eliminate boundary layer development in the investigation domain. There is also a sixth plate immediately prior to the test section to promote flame acceleration. The turbulence generator is followed by a 150 mm long test section. This section offers 102 mm of optical access via two 25 mm thick fused silica windows. Additionally, the test section houses another pane of quartz on the bottom for planar measurements and five piezoelectric pressure transducers along the top of the section for high-frequency pressure measurements. The test section is followed by a 610 mm straight open channel that exhausts to ambient conditions.

Facility operation begins with filling the TST with a reactant mixture. The reactant mixture used in this experiment was hydrogen-air at varying equivalence ratios ($\Phi = 0.84, 0.92, 0.96$). Compressed gasses were regulated from compressed gas tanks to a pressure of 50 psi. After regulation, the fuel and air flow rates are controlled with two Dwyer VFA-4 rotameters with an uncertainty of \pm 0.1 SCFH. The fuel and air are mixed upstream of the facility and passes through several feet of polyurethane tubing and a three-way MAC solenoid. After the solenoid, the flow separates into an array of eight polyurethane tubes to promote homogenous mixing. Here, the flow enters the facility where it fills for 20 s to ensure a homogeneous mixture fills the TST [10,22]. After the 20 second fill time, a BNC 575 pulse/delay generator is used to ignite the mixture and synchronize the high-speed diagnostic systems.

2.2. Diagnostics

A suite of high-speed optical diagnostics are simultaneously employed to study turbulent compressible flames: high-speed schlieren, OH* chemiluminescence, PIV, and pressure transducer measurements. An overview of this diagnostic setup is

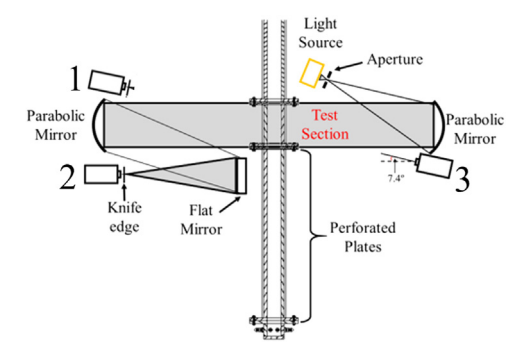


Fig. 2. Schematic of the optical diagnostics setup for simultaneous high-speed PIV, schlieren, and OH* imaging.

shown in Fig. 2. In Fig. 2, the camera notations are as follows: (1) chemiluminescence, (2) schlieren, and (3) PIV. To allow for simultaneous measurements, the cameras recording PIV and chemiluminescence data are set to a seven-degree angle with respect to the line of sight. Measurements are corrected for the angle projection. Further explanations of the measurements are provided below. An overview and the overlap of the field of view for each of the measurement domain is displayed in Fig. 1.

PIV data is collected to investigate flow field characteristics. A Nd:YAG Lee Laser LDP Dual Laser (532 nm, 25 mJ) is operated at 50 kHz with the light sheet focused in the center of the test section. During the fill portion, 30 nm Al₂O₃ particles are seeded into the flow [28]. The PIV data is then collected via a Photron SA-Z recording at 100 kHz with a resolution of 768 × 240 pixels for framestraddled PIV. A Nikon 300 mm focal length, f/2.8 lens with a 20 mm extension tube is attached to the camera for the PIV measurements. The resulting field of view is 51 × 19 mm with a vector resolution

Table 1 Experimental conditions.

Φ	P/P _{CJ}	u' _{rms} (m/s)	Flame Classification
0.84	0.45	42	Slow Deflagration $(S_T < S_{CJ})$
0.92 0.96	0.63 0.99	70 109	Fast Deflagration ($S_T \sim S_{CJ}$) Choked Flame ($S_T > S_{CJ}$)
			(-1 - 0)

of 26.56 μ m. The data is processed in commercial software (LaVision DaVis 10) using a two-step, six pass investigation; the final interrogation window is 16×16 -pixels, and a 75% overlap was used for each pass.

Chemiluminescence data is used to extract the flame front. This experiment collected OH* measurements with a Photron SA-1 equipped with a 50 mm Nikon lens (f/1.4). The data is recorded at 50 kHz with a resolution of 512 × 208 pixels. OH* measurements were captured in a 53 × 22 mm window and collected simultaneously with the PIV measurements. The spatial uncertainty is $104 \ \mu \text{m/pix}$. The flame front was then extracted using a Canny Edge detection algorithm in MATLAB software [10,11,25-27].

Additionally, schlieren data was collected to visualize the shock, compressed region, and flame characteristics. For this experiment traditional Z-schlieren was implemented with a Newport 300 W lamp, along with two six-inch collimating mirrors (focal length = 60 inches), and a third two-inch converging mirror. The light was cut with a knife edge on the left, resulting in higher densities appearing as bright regions. The schlieren is recorded with a Nikon 200 mm f/2.8 lens attached to a Photron SA-Z. Images are collected at a rate of $100 \, \text{kHz}$ at a resolution of 512×208 with a 12-bit depth range. The examined field of view is 46×18 mm with a resulting spatial uncertainty of $89 \, \mu \text{m/pix}$ and a shock-based velocity uncertainty of $8.9 \, \text{m/s}$.

Finally, pressure measurements are recorded to quantify various regions of flow. A series of five PCB pressure transducers (Model #113B26) are evenly spaced 25 mm apart in the axial direction. The pressure measurements are collected at 1.25 MHz, with a sensitivity of 10 mV/psi. Two PCB 482C Series signal conditioners are used to amplify the measurements before being sent to an NI DAQ for LabVIEW processing.

2.3. Test conditions

The conditions explored for this study are provided in Table 1. Three different equivalence ratios are investigated to span different compressible flame regimes, and each condition is repeated five times to ensure results are repeatable. The average case for each equivalence ratio is discussed. An overview of these data sets is depicted on the turbulent flame regime diagram in Fig. 3. Specifically,

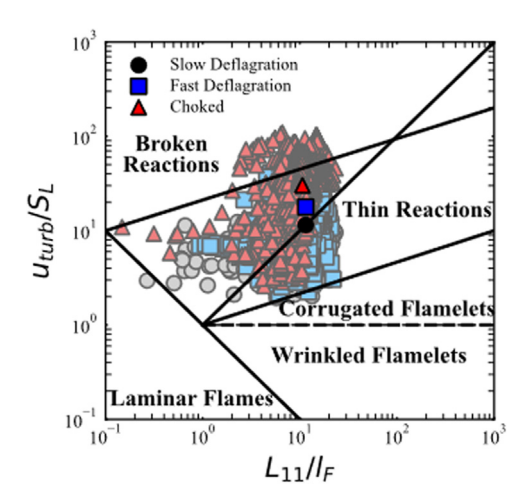


Fig. 3. Premixed turbulent regime diagram with the mean values for each test case plotted as solid points in the foreground.

all data in Fig. 3 was obtained at the time instant where the flame was centered in the investigation domain. The ensemble of transparent points in the background represents the distribution of all u'_{rms} and L_{11} across the flame front, and the solid points in the foreground represent the mean values. Additional mean quantities for each case is provided in Table 1 [29]. As shown in Fig. 3, there is little variance in the integral length scales; however, the turbulence velocity fluctuations directly ahead of the flame vary significantly with increasing equivalence ratios.

3. Results

The resulting measurements provide insights into turbulent compressible flame dynamics that ultimately lead to DDT. The results leverage flame imaging and flow field measurements to provide insights of flame-vortex interactions and the relationship to DDT. Through examining both planar and line-of-sight measurements, the mechanisms that drive flame generated turbulence are explored.

Schlieren measurements are presented to visualize different turbulent flame compressibility regimes. A sample for each flame regime is presented in Fig. 4. Fig. 4a displays a subsonic flame representing the slow deflagration regime. It is evident in this regime that the shock and the compressed region do not influence the flame and flow behavior due to the large separation between the shock and flame front. The fast deflagration case is shown in Fig. 4b. As the equivalence ratio increases, the shock and the flame become closer together, and small regions of flame generated compression are noticed ahead of the flame front. The compressed region is denoted by the dashed shaded

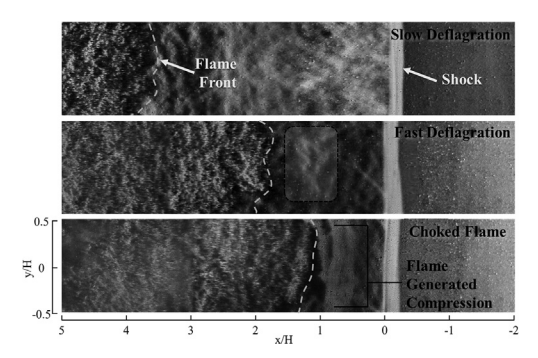


Fig. 4. Schlieren visualization of different compressible flame regimes obtained from the three test conditions.

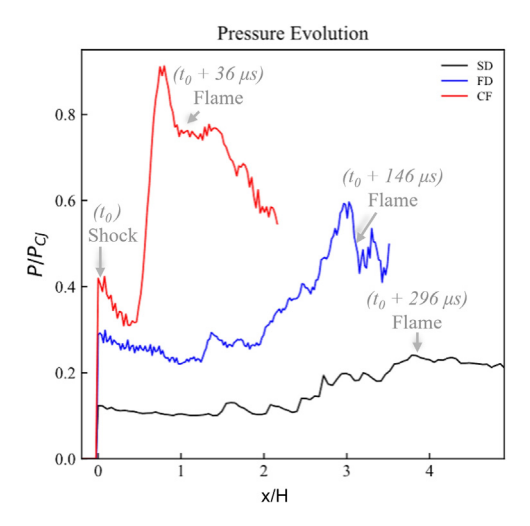


Fig. 5. Pressure profiles for the slow deflagration (SD), fast deflagration (FD), and choked flame (CF) conditions.

region. In Fig. 4c, a choked flame is shown, revealing a significant band of compression coming directly from the flame. There is minimal distance between the shock and the flame resulting in high pressures within the compressed region.

The compressed region is quantified via highspeed pressure measurements. Fig. 5 shows the pressure characteristics of the three compressible regimes explored. Since the high-speed imaging provides knowledge of the spatial and temporal evolution of the shock and flame, the pressure profiles can be recast into spatial profiles with respect to the leading shock. Additional details of the method can be found in literature [26,27]. In Fig. 5, the pressure profiles are presented as a function of x/H; here, H = 45 mm is the height of the channel, and x = 0 is marked at the location of the leading normal shock. t_0 denotes the arrival time of the shock at the second transducer. The time is also noted for the arrival of the flame as a function of $t_0 + t$ (see Fig. 5).

The slow deflagration case reveals little to no compression ahead of the flame after a steady build up from the normal shock. The following fast deflagration regime occurs on a much shorter timescale, with the shock and flame measured to be 146 μ s apart. In this trace, there is evident isotropic compression behind the shock leading to a slightly compressed region directly ahead of the flame front. The choked evolution shows strong evidence of flame generated compression. The Mach 2.4 shock generates compression in the first 0.5*H*. However, in the following 0.5H the pressure triples to a peak pressure of 0.91 P/P_{CJ} (15 atm). The magnitude and timescale of this pressure rise is unlike the previous two cases and correlates strongly to the increased density band produced by the flame (also shown visually in Fig. 4c). In this scenario, the shock and flame are closely coupled sitting only 36 μ s apart.

While schlieren shows the visual region of compression and pressure measurements provide quantification of this compression, the chemiluminescence and PIV measurements offer perspective into the flow and flame behavior. Since turbulence and vorticity are coupled, it is important to examine the driving mechanisms of vorticity generation within the compressed region and flame. The streamwise velocity and vorticity field with the corresponding flame structure overlaid are presented in Fig. 6. In Fig. 6a, it is evident that as the equivalence ratio increases there is a corresponding increase in the streamwise velocity. The velocity fields are presented using a coordinate system which begins with x/H = 0 as the leading shock. The velocity and vorticity fields presented are near the flame to examine the flame and flow-field interactions. As previously noted in Fig. 5, the flame front is significantly closer to the leading shock within the choked flame regime $(x/H \approx 0.7)$ when compared with the other flame regimes. In the slow deflagration case, there are minimal velocity changes throughout the flame front, and the vorticity changes constantly throughout the reactants and products. In contrast, there is a notable increase in flow velocity from reactants to products in the fast deflagration case. In this regime, the vorticity starts to become more prevalent in the reactants ahead of the turbulent flame, likely from the beginning stages of flame generated compression. In the case of the choked flame, the flame front profile is nominally flat. However, locally, the flame has increased wrinkling likely due to the interaction of the flame with the strong turbulent vorticity generated in the compressed region. In this case, there are high velocity magnitudes in front of the flame, which match the order of the velocity in the product region. Additionally, the magnitude of the vorticity is high within the compressed region, as well as in local areas immediately succeeding the flame. Like the fast deflagration case, the vorticity after the flame decreases. These contours confirm common

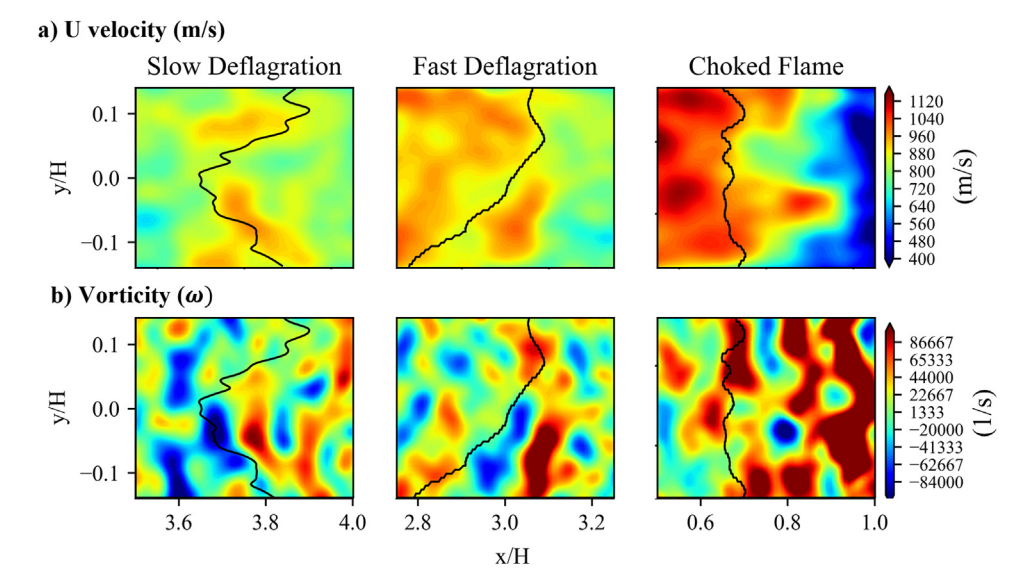


Fig. 6. Instantaneous flow field contours and corresponding flame front. (a) Streamwise velocity and (b) span-wise vorticity for the slow deflagration, fast deflagration, and choked flame.

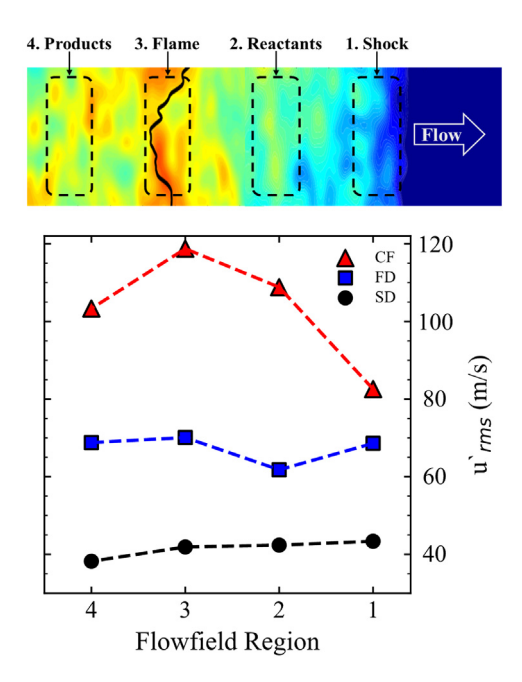


Fig. 7. (a) An example of a turbulent flow field and regions of interest, (b) u'rms characteristics throughout the regions of interest: shock, reactants, flame, products.

flow characteristics while showing increased vorticity ahead of the highly turbulent flame.

The local turbulent velocity fluctuations are examined for the turbulent flame regimes. Fig. 7a and b display u'_{rms} throughout the shock, reactants,

flame region, and products. These regions capture the effect of flame compressibility on turbulence generation. The u'_{rms} used in these measurements is defined using Eq. (1).

The turbulent velocity in the horizontal direction is isolated by subtracting the local mean convective velocity (\bar{u}). The u'_{rms} is computed using a 4×4 grid throughout the flow [10,22,25]. The mean of both the u' and v' velocities behind the leading shock and throughout the flow are confirmed to be zero.

$$w(x, y) = \sqrt{\frac{1}{|2N_i| \times |2N_k|} \sum_{i=\pm 1}^{N_i = \pm 2} \sum_{k=\pm 1}^{N_k = \pm 2} [u(x_i, y_k) - \bar{u}(x_i, y_k)]}^2}$$

$$where w = w(x, y). \tag{1}$$

The slow deflagration regime, depicted in Fig. 7b, has nominally constant turbulence throughout the entire flow field with a minor decrease in the products region, which is expected due to the temperature dependent turbulent viscosity. The fast deflagration experiences an increase in turbulence, however in contrast to the slow deflagration there is an increase in the turbulence at the flame front indicating the beginning of flame generated turbulence influencing the flow field. The choked flame has a significantly different distribution of turbulent fluctuations when compared to the other regimes. This is demonstrated by the continuously increasing turbulence values through the compressed region to the flame. This is a result of flame generated compression region, first shown

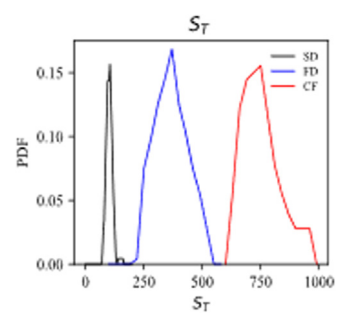


Fig. 8. Probability density function (PDF) of turbulent flame speed for all explored conditions.

visually in Fig. 3, causing significant changes to the flow field. There are key characteristics contributing to the proximity of DDT in the choked flame case. As the flame approaches the shock, the gas becomes more compressed.

The role of flame generated compression is ultimately explored through the turbulent flame speed. The turbulent flame speed, S_T , predicts the possibility of the turbulent flame runaway mechanism that leads to the onset of DDT. In addition, S_T can be used to highlight the compressibility effects as the value approaches the CJ deflagration speed. The turbulent flame speed is quantified as $S_T = V_f - V_g$, where V_f is the propagation speed of the flame determined from the OH* images, and V_g is the gas velocity at the flame front.

In Fig. 8, the PDF's of the turbulent flame speeds across the flame front are compared for the three regimes. The corresponding CJ deflagration velocity averages around 292 m/s for the three mixtures. The mean turbulent flame speed for the slow deflagration is $S_T = 110$ m/s and the range of S_T values are highly concentrated near the mean. This is a result of the low turbulence fluctuations and steady propagation values witnessed in this regime. The fast deflagration averages at $S_T = 280$ m/s. This regime is near surpassing the theoretical CJ deflagration value, and supports the slight compression revealed in Fig. 6. Finally, the choked flame has an average turbulent flame speed of 700 m/s. At this location, nonlinear compressibility is known to govern the flame front dynamics, which provides favorable conditions for the onset of DDT. The wider distribution of S_T for the fast deflagration and choked flames are a result of higher heat release, which drives an increase in pressure as previously noted in Fig. 5. The pressure rise will increase the local pressure gradients in the flow field, which will couple with acute density gradients in the post shock region to generate turbulence from the baroclinic torque mechanism. Thus, the turbulence upstream of the flame is largest for the choked flame case, and ultimately results in the wider distribution of the turbulent flame speed.

4. Conclusion

The role of flame generated compression in the DDT process is experimentally quantified through direct flow field measurements. More specifically, higher turbulent flame speeds are proven to contribute significantly to overall flame acceleration. High turbulence fluctuations and regions of flow compression ahead of the flame are commonly attributed to increased baroclinic torque production. This mechanism is driven by flame generated compression in the reactants, which produces turbulence ahead of the flame from misaligned density and pressure gradients. This work alludes to the greater concept of baroclinic torque production drive the DDT process.

Ultimately, this work offers insight into the direct role of flame generated compression to the deflagration to detonation transition process. The work provides multiple areas of evidence both quantitatively and qualitatively, that heightened compression ahead of flame repeatedly attributes to DDT shortly after. Finally, the work experimentally connects the compression generated by the flame front to the measured increased vorticity also experienced by the flow field.

Declaration of competing interest

The authors declare that they have no known competing financial interests or personal relationships that could have appeared to influence the work reported in this paper.

Acknowledgements

This work is sponsored by the Air Force Office of Scientific Research (FA9550–16–1–0403 and FA9550–19–1–0322; Program Manager Dr. Chiping Li), the National Science Foundations (NSF Award #1914453), and the American Chemical Society Petroleum Research Fund (54753–DNI).

References

- [1] A. Khokhlov, A theory of deflagration-to-detonation transition in unconfined flames, Combust. Flame 108 (4) (1997) 503–517.
- [2] E.S. Oran, Astrophysical combustion, Proc. Combust. Inst. 30 (2) (2005) 1823–1840.
- [3] V.N. Gamezo, The influence of shock bifurcations on shock-flame interactions and DDT, Combust. Flame (126) (2001).
- [4] D. Bradley, M. Lawes, K. Liu, Turbulent flame speeds in ducts and the deflagration/detonation transition, Combust. Flame 154 (1–2) (2008) 96–108.
- [5] M.A. Liberman, M. Kuznetsov, A. Ivanov, I. Matsukov, Formation of the preheated zone ahead of a propagating flame and the mechanism underlying the

- deflagration-to-detonation transition, Phys. Lett. A 373 (5) (2009) 501–510.
- [6] M. Saif, W. Wang, A. Pekalski, M. Levin, M.I. Radulescu, Chapman–Jouguet deflagrations and their transition to detonation, Proc. Combust. Inst. 36 (2) (2017) 2771–2779.
- [7] X. Lu, C.R. Kaplan, E.S. Oran, Predictions of flame acceleration, transition to detonation, and detonation propagation using the Chemical-Diffusive model, Combust. Flame (2021).
- [8] M. Kuznetsov, M. Liberman, I. Matsukov, Experimental study of the preheat zone formation and deflagration to detonation transition, Combust. Sci. Technol. 182 (11–12) (2010) 1628–1644.
- [9] P.B. Venkatesh, High-pressure combustion and deflagration-to-detonation transition in Ethylene/Nitrous oxide mixture, 8th U. S. National Combustion Meeting, 2013.
- [10] J. Sosa, J. Chambers, K.A. Ahmed, A. Poludnenko, V.N. Gamezo, Compressible turbulent flame speeds of highly turbulent standing flames, Proc. Combust. Inst. 37 (3) (2019) 3495–3502.
- [11] H.M. Chin, J. Chambers, J. Sosa, A. Poludnenko, V.N. Gamezo, K.A. Ahmed, The evolution of pressure gain in turbulent fast flames, Combust Flame 234 (2021) 111641.
- [12] P. Krivosheyev, O. Penyazkov, A. Sakalou, Analysis of the final stage of flame acceleration and the onset of detonation in a cylindrical tube using high-speed stereoscopic imaging, Combust. Flame 216 (2020) 146–160.
- [13] G. Ciccarelli, S. Dorofeev, Flame acceleration and transition to detonation in ducts, Prog. Energy Combust. Sci. 34 (4) (2008) 499–550.
- [14] J. Li, W.H. Lai, K. Chung, F.K. Lu, Experimental study on transmission of an overdriven detonation wave from propane/oxygen to propane/air, Combust Flame 154 (3) (2008) 331–345.
- [15] T. Ogawa, E.S. Oran, V.N. Gamezo, Numerical study on flame acceleration and DDT in an inclined array of cylinders using an AMR technique, Comput. Fluids 85 (2013) 63–70.
- [16] C. Wang, Y. Zhao, B. Zhang, Numerical simulation of flame acceleration and deflagration-to-detonation transition of ethylene in channels, J. Loss Prev. Process Ind. 43 (2016) 120–126.
- [17] C. Wang, J. Guo, K. Zhang, S. Du, H. Chen, F. Yang, Experiments on duct-vented explosion of hydrogen-methane-air mixtures: effects of equivalence ratio, Fuel 308 (2022) 122060.

- [18] C. Wang, Y. Zhao, W. Han, Effect of heat-loss boundary on flame acceleration and deflagration to-detonation transition in narrow channels, Combust, Sci. Technol. 189 (9) (2017) 1605–1623.
- [19] H. Wang, et al., A physics-based approach to modeling real-fuel combustion chemistry - I. Evidence from experiments, and thermodynamic, chemical kinetic and statistical considerations, Combust. Flame 193 (2018) 502–519.
- [20] E.S. Oran, Understanding explosions From catastrophic accidents to creation of the universe, Proc. Combust. Inst. 35 (1) (2015) 1–35.
- [21] A.Y. Poludnenko, T.A. Gardiner, E.S. Oran, Spontaneous transition of turbulent flames to detonations in unconfined media, Phys. Rev. Lett. 107 (5) (Jul 29 2011) 054501.
- [22] A.Y. Poludnenko, J. Chambers, K. Ahmed, V.N. Gamezo, B.D. Taylor, A unified mechanism for unconfined deflagration-to-detonation transition in terrestrial chemical systems and type Ia supernovae, Science 366 (6465) (Nov 1 2019).
- [23] J. Sosa, Supersonic Driven Detonation Dynamics for Rotating Detonation Engines, Int. J. Hydrogen Energy (2018).
- [24] M.I. Radulescu, A detonation paradox: why inviscid detonation simulations predict the incorrect trend for the role of instability in gaseous cellular detonations? Combust. Flame 195 (2018) 151–162.
- [25] J.P. McGarry, K.A. Ahmed, Flame-turbulence interaction of laminar premixed deflagrated flames, Combust. Flame 176 (2017) 439–450.
- [26] J. Chambers, K. Ahmed, Turbulent flame augmentation using a fluidic jet for Deflagration-to-Detonation, Fuel 199 (2017) 616–626.
- [27] J. Chambers, K.A. Ahmed, L.R. Oneill, A. Poludnenko, and V.N. Gamezo, "Evidence of pressure build-up in H2-Air Fast Flames for Deflagration-to-Detonation," presented at the AIAA Scitech 2019 Forum, 2019.
- [28] S.S. Dammati, Y. Kozak, C. Rising, J. Reyes, K.A. Ahmed, A.Y. Poludnenko, Numerical investigation of the accuracy of particle image velocimetry technique in gas-phase detonations, Proc. Combust. Inst. 38 (3) (2021) 3671–3681.
- [29] Poinsot, Diagrams of premixed turbulent combustion based on direct simulationTwenty-Third Symff.Jsium (International) on Combustion, 1990.